Research Article | Vol. 28, No. 10 / 11 May 2020 / Optics Express 15587
Optics EXPRESS

Hard-wired lattice light-sheet microscopy for imaging of expanded samples

ANNE STOCKHAUSEN,[1,5] JANA BÜRGERS,[1,5] JUAN EDUARDO RODRIGUEZ-GATICA,[1] JENS SCHWEIHOFF,[2] RUDOLF MERKEL,[3] JENS MARKUS PRIGGE,[4] MARTIN KARL SCHWARZ,[2] AND ULRICH KUBITSCHECK[1,*]

[1]*Institute of Physical and Theoretical Chemistry, University of Bonn, Wegelerstr. 12, 53115 Bonn, Germany*
[2]*Institute for Experimental Epileptology and Cognition Research (EECR), University of Bonn Medical School, Sigmund-Freud-Str. 25, 53127 Bonn, Germany*
[3]*Institute of Biological Information Processing 2: Mechanobiology, Forschungszentrum Jülich GmbH, 52425 Jülich, Germany*
[4]*Institute of Biological Information Processing: Mechanics Workshop, Forschungszentrum Jülich GmbH, 52425 Jülich, Germany*
[5]*These authors contributed equally to this research*
[*]*u.kubitscheck@uni-bonn.de*
https://www.chemie.uni-bonn.de/pctc/kubitscheck

Abstract: Light-sheet fluorescence microscopy (LSFM) helps investigate small structures in developing cells and tissue for three-dimensional localization microscopy and large-field brain imaging in neuroscience. Lattice light-sheet microscopy is a recent development with great potential to improve axial resolution and usable field sizes, thus improving imaging speed. In contrast to the commonly employed Gaussian beams for light-sheet generation in conventional LSFM, in lattice light-sheet microscopy an array of low diverging Bessel beams with a suppressed side lobe structure is used. We developed a facile elementary lattice light-sheet microscope using a micro-fabricated fixed ring mask for lattice light-sheet generation. In our setup, optical hardware elements enable a stable and simple illumination path without the need for spatial light modulators. This setup, in combination with long-working distance objectives and the possibility for simultaneous dual-color imaging, provides optimal conditions for imaging extended optically cleared tissue samples. We here present experimental data of fluorescently stained neurons and neurites from mouse hippocampus following tissue expansion and demonstrate the high homogeneous resolution throughout the entire imaged volume. Utilizing our purpose-built lattice light-sheet microscope, we reached a homogeneous excitation and an axial resolution of 1.2 µm over a field of view of (333 µm)^2.

1. Introduction

In the past years, light-sheet fluorescence microscopy (LSFM) revolutionized light microscopic imaging in developmental biology of mammals, insects and plants [1] but also in three-dimensional localization microscopy and large field brain imaging in neuroscience [2,3].

In marked contrast to epi-illumination microscopy in LSFM fluorescence excitation and detection occur along orthogonally arranged beam paths. Typically, the sample is illuminated by a thin sheet of light, which is either stationary and generated by a cylinder lens, or generated by scanning a thin excitation beam. This approach enables fast imaging of an entire illuminated plane, which is in the focus of a detection objective lens and visualized by a sensitive CCD or CMOS camera. Thus LSFM features intrinsic optical sectioning and low photobleaching, since fluorescence excitation and photobleaching are confined to a single object plane. Moreover, image contrast is significantly better compared to epi-illumination microscopy and is further

#393728 https://doi.org/10.1364/OE.393728
Journal © 2020 Received 26 Mar 2020; revised 27 Apr 2020; accepted 28 Apr 2020; published 7 May 2020

Optics EXPRESS

improved by using the scanned laser beam configuration for illumination and synchronized line detection, which produces a confocal line detection scheme [4,5].

Initially, scanned light-sheets were generated with classical Gaussian beams [6], but recently also two-photon excitation [7], Bessel [8,9], Airy [10] beams, or even stimulated excitation-depletion (STED) excitation [11] were introduced (for review, see [12]). Briefly, Gaussian beams are straightforward to produce, but their useful Rayleigh length in propagation direction is related to the square of their diameter and thus resulting in a marked reduction of the actual illumination field. Two photon excitation beam profiles are spatially quite confined, however, the instrumentation is fairly expensive. Airy beams are similarly constant along their propagation direction, however, suffer also from strong side lobes. STED excitation is spatially extremely confined, but the required laser setup is complex and expensive. Moreover, it is not compatible with all combinations of fluorescent dyes. Bessel beams are self-reconstructive and have a thin main maximum, which is however surrounded by relatively strong side lobes, which lead to a high out-of-focus contribution.

A few years ago, Eric Betzig and coworkers introduced lattices of Bessel beams as an alternative excitation mode [13]. In their setup a spatial light modulator was used to generate a lattice of Bessel beams that were so close to each other that the side lobes interfered destructively, thus minimizing out of focus contributions. Importantly the Bessel beams retained their feature of being self-reconstructive, which lead to a significantly extended axial range in beam propagation direction. The resulting light lattice could either be swept across the object plane for creating a light-sheet, or alternatively used to increase the axial resolution by moving the lattice step-wise, creating a structured illumination microscopy mode. This instrument setup featured high imaging frame rates and a superior axial resolution and was optimally adjusted to examine small transparent objects. In a previous project we demonstrated the use of classical LSFM to image sections of mouse brain slices following tissue expansion [14]. Tissue expansion allowed us to optically resolve fluorescent structures spaced closer than the optical diffraction limit yielding effective super resolution images. As a result the achieved effective resolution and overall image quality was superior compared to classically cleared tissue imaged by LSFM. However, the large samples size afforded imaging in a mosaic-like fashion. The converging/diverging character of Gaussian beams further reduced the usable field of view for each mosaic tile.

Thus, to increase axial resolution across the excitation field and reduce out-of-focus excitation as well as imaging time of large expanded samples at high resolution we here implemented lattice light-sheet microscopy (LLSFM). LLSFM is ideally suited for this purpose due to the formation of partly self-reconstructive illumination beams leading to larger imaging fields. We here present a purpose-built instrument that provides robust and rapid imaging, especially for transparent extended samples. We report on the construction of this imaging instrument, the quantitative characterization of its optical features and finally its application in imaging expanded mouse brain section samples revealing critical details of neuronal networks.

2. Methods

In any microscope the light pattern in the front focal plane of a lens is determined by the light pattern in the back focal plane of the objective. Both distributions are related to each other by a Fourier transformation. In light-sheet microscopy illumination and detection occur by two distinct objective lenses. Thus, we defined the illumination light pattern in the sample space by placing a defined mask into a plane conjugated to the back focal plane of the illumination objective. The theoretically expected illumination light pattern was calculated using discrete fast Fourier transformation algorithms from MATLAB (Version R2014a, The MathWorks, Inc., Natick, Massachusetts, United States). An infinitely thin ring pattern in the back focal plane results in a Bessel beam along the illumination axis (x-direction). Inspired by Chen et al [13]. we considered a mask featuring thin vertical slots confined on a ring. As demonstrated by Chen

Optics EXPRESS

et al. ([13], also, see [15]) and our own simulations this leads to a confined optical lattice in the sample plane, whose individual beams are low-diverging Bessel-Gaussian beams. The final result is defined by the parameters of the slit mask, namely the outer diameter of the ring, D_1, its width, d, the number, A, and the width of the slits, T. A finite ring width causes the formation of mixed Bessel-Gaussians beams, which are not completely propagation-invariant like perfect Bessel beams. The number of slits defines the density of the Fourier pattern in the sample space. To generate a homogeneous pattern in the sample plane it is optimal to employ a small number of slits. The lattice pattern is thinner in the direction of the detection beam path (z-direction), if the outermost slits in the mask are tangential to the inner radius of the ring. For these certain distances of the slits the side lobes of the Bessel beams in the lattice interfere efficiently in a destructive manner. The slit width T is inversely related to the width of the overall beam lattice. For a wide lattice achieving illumination of a large object field a small slit width should be chosen. Obviously, this simultaneously limits the light transmission efficiency of the mask.

We decided to use a mask with three slits as shown in Fig. 1. The MATLAB simulation allowed to compute the resulting light distribution in the illumination plane. Program input are the ring parameters, D_1 and d, and the slit parameters, T and A, respectively (Fig. 1(a)). The resulting image, which shows the defined slits confined to the specific ring (Fig. 1(b)), is transformed into a binary 4000×4000 matrix. The matrix entries are set to unity at the light transmitting slit positions and to zero elsewhere. This matrix is two dimensionally Fourier transformed using the function *fft2* and squared to compute the intensity of the optical lattice (Fig. 1(c)). In this way, the expected light pattern of the lattice light-sheet can be simulated.

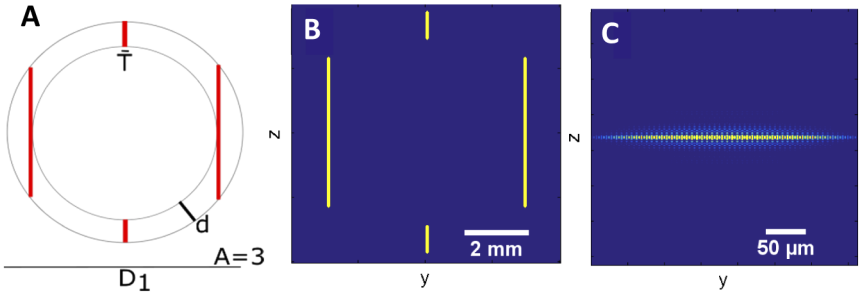

Fig. 1. Mask with three slits. (a) Definition of mask parameters. (b) Sketch of the mask with D_1=7.5 mm, d=0.8 mm, width T=100 µm. (c) Simulated intensity distribution in the central maximum of the diffraction pattern.

The mask was produced in a precision mechanics workshop using a computerized numerical control (CNC) milling machine (DMC 650 V, DMG Mori, Bielefeld, Germany) equipped with a solid carbide miniature end mill (VHM 0.1 mm diameter, Karnasch, Heddesheim, Germany). This machine enabled to create slits with a minimum width of 100 µm in an aluminum plate. The complete beam path of the microscope is shown in Fig. 2.

We used two separate illumination beam paths that allowed us to directly compare the properties of the lattice light-sheet and a Gaussian beam illumination. The illumination arm on the left-hand side generated the lattice light-sheet illumination. The incoming laser beams originating from a laser hub (C-FLEX, Hübner Photonics, Kassel, Germany) emitting laser lines at 405, 488, 561 and 638 nm were brought to the instrument by an optical monomode fiber. The incoming light passed a λ/2 plate and was split by a polarizing beam splitter. Typically, an excitation power of 70 mW per laser line – measured behind the beam splitter – was used. On the right-hand side a normal illumination beam path using a scanned Gaussian beam was assembled [14]. For focusing the beam into the sample, we used an air objective lens (10x, numerical aperture (NA) 0.28, working distance (WD) 33.5 mm, Mitutoyo, Mitutoyo Corp., Kawasaki, Japan). In the

Optics EXPRESS

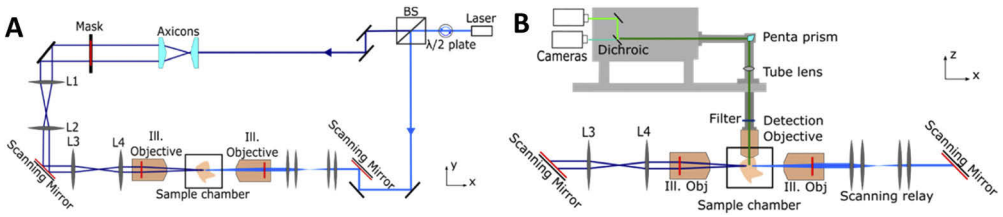

Fig. 2. Setup of the lattice light-sheet microscope. (a) Top view of the illumination beam path comprising the mask (upper section and left) and the Gaussian illumination (right-hand side). Conjugate planes were marked in red. (b) Side view of the instrument showing the detection beam path.

second beam path we used two axicons (AX2510-A, Thorlabs, Bergkirchen, Germany) to create a ring-shaped beam profile. The diameter of the ring profile is defined by the distance between the axicons. The resulting ring beam illuminated the mask. Without the axicons, the major part of the illumination beam would be blocked by the mask. Still, the light loss at the mask amounted to 93.5%. The lenses L1 (f=100 mm) and L2 (f=50 mm) mapped the mask onto the scanning mirror, which dithered the lattice pattern, and de-magnified it by a factor of 2. Two final lenses L_3 and L_4 (f = 75 and 60 mm, respectively; all lenses from Thorlabs) imaged the dithered mask pattern into the back focal plane of the illumination objective (10x, NA 0.28, WD 33.5 mm, Mitutoyo). Here, typically laser irradiances of 4 mW were measured. The conjugate planes of the mask are marked in red in Fig. 2(a). The scanning mirror, the lenses L_3 and L_4, as well as the illumination objective were mounted on a linear stage (LNR50K1/M, Thorlabs) to enable the adjustment of the lattice foci with respect to the detection axis.

The light lattice was formed in a custom-built, water-filled sample chamber. The chamber featured entrance windows at both sides with a thickness of 170 µm. The biological specimen itself was fixed by poly-L-lysine on a coverslip, which could be moved on a handle in three spatial directions by individual computer-controlled step motors (Micro Translation Stage M-112.1DG, Physik Instrumente GmbH, Karlsruhe, Germany) to allow automatic image acquisition from any sample location. To image biological samples, the pH value of the solution in the chamber was adjusted to 7.4 to improve fluorophore stability.

For light detection, we used a water dipping objective lens (40x, NA 1.0, Carl Zeiss Microscopy, Jena, Germany) with a WD of 2.5 mm. A tube lens changer allowed to introduce an optional magnification of 1.6. A set of Notch filters centered at the respective excitation wavelengths filtered the emitted fluorescence light, which was guided by a pentaprism into a beam splitter device (W-View Gemini-2C, Hamamatsu Photonics K. K., Hamamatsu City, Japan). The latter allowed to image two different fluorescence channels simultaneously by two sCMOS cameras (Orca Flash 4.0 V3, Hamamatsu Photonics) featuring 2048×2048 pixels with a pixel size of 6.5 µm. Using the 40x magnification the field of view amounted to $(333\,\mu m)^2$ with an object pixel size of 162.5 nm. This pixel size fulfilled the Nyquist condition for green, yellow and red fluorescence, but not for blue. The use of the second tube lens, however, reduced the object field pixel size to 101.6 nm, which was well beyond the Nyquist limit for all fluorescence channels. The complete instrument was governed by a custom-developed LabVIEW software (National Instruments, Austin, Texas, USA) for directing the laser hub, scanners, cameras and motors. It allowed live image display and tiled image stack acquisition.

Optics EXPRESS

3. Results

3.1. Illumination pattern

The mask produced the expected diffraction pattern in the sample representing a grid of parallel light beams. The grid could be observed by illuminating the sample chamber filled with a diluted fluorescein solution and imaging the stationary pattern (Fig. 3). Computed and measured illumination light distribution differed mostly by a broad background in the latter. This was created by out of focus light registered by the camera. The distances between the lattice maxima $d_{exp} = (3.4 \pm 0.2)$ µm observed in the fluorescein solution agreed with the simulation-predicted values, $d_{sim} = 3.2$ µm within the standard deviation. We assume that the observed deviations were due to small imperfections in the produced mask and optical aberrations in the illumination beam path.

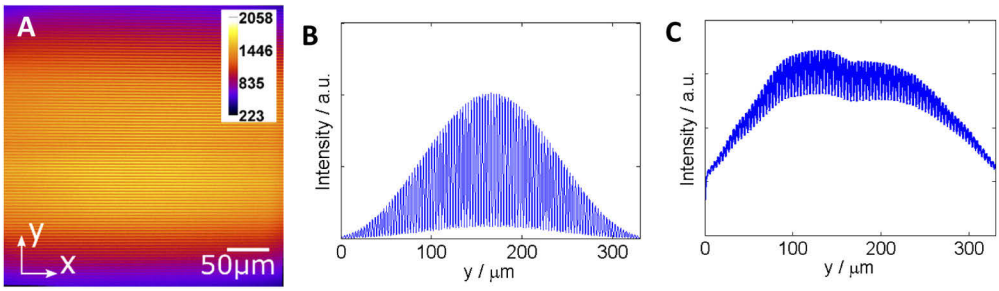

Fig. 3. Optical lattice produced in the sample chamber. (a) Image of the lattice over a field of $(333\,\mu m)^2$. (b) Theoretically calculated intensity distribution in y-direction. (c) Intensity profile in y-direction from Fig. 3(a).

3.2. Variation of excitation wavelength

Comparable diffraction patterns were produced by laser lines exhibiting different wavelengths. For demonstration, water solutions containing Alexa Fluor 532 and Alexa Fluor 647 were prepared and illuminated (Fig. 4). The distances between the maxima and their widths increased linearly with increasing wavelength from 488 nm, over 561 nm to 638 nm as theoretically expected. Similarly, the position of the beam waists in the illumination (x-) direction depends on the excitation wavelength. We adjusted the linear stage that contained a part of the illumination beam path such that the 561 nm laser beam waist was positioned at the location of the detection beam path. The 488 nm laser focus was shifted 10 µm to the left and the 638 nm focus was shifted 12 µm to the right.

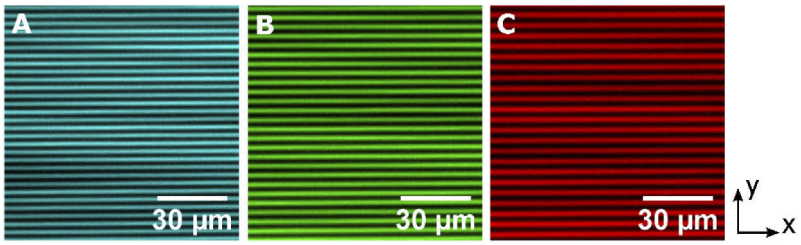

Fig. 4. Optical lattices produced in the sample chamber using different excitation wavelengths over a field of $(100\,\mu m)^2$ for an excitation wavelength of (a) 488 nm, (b) 561 nm, and (c) 638 nm.

Optics EXPRESS

Notably, due to the design of a light-sheet microscope the lattices of all three excitation lasers are positioned in a single plane with regard to the detection axis, which is advantageous for simultaneous multicolor imaging.

3.3. Resolution and illumination field size

The convergence and divergence of the Gaussian illumination beam beyond the focus region is a clear disadvantage of classical LSFM, especially when imaging extended samples [14]. A propagation-invariant Bessel beam illumination can definitely improve this situation [8,9]. We therefore expected an improved axial uniformity of the illumination field as a key feature of lattice illumination. In addition, the axial extension of a Bessel lattice is reduced compared to that of a Gaussian beam, resulting in an increased axial resolution across the excitation field and a reduced out-of-focus excitation [13].

For Gaussian beams the usable field width corresponds approximately to twice the Rayleigh length, L_R, of the beam, see below. Beyond this region the divergence of the beam leads to a strong decrease in the optical sectioning capability of the setup. We compared usable illumination field sizes of two different Gaussian beams and of lattice illumination.

To this end we chose Gaussian beams with narrow and wide beam waists, $\omega_{0,n}$ and $\omega_{0,w}$, respectively, with a wavelength of 488 nm. The beam intensity profiles were visualized using the fluorescence that was excited by the stationary beams in a diluted fluorescein solution by means of the sCMOS camera (Figs. 5(a) and (b)).

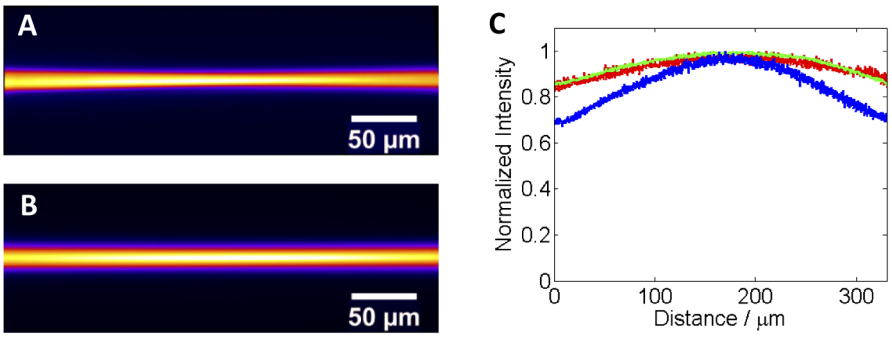

Fig. 5. Images of the various illumination fields imaged in fluorescein: (a) Narrow Gaussian beam, (b) wide Gaussian beam. The narrow beam resulted from a two-fold expansion of the wide Gaussian beam before the illumination objective, what results in a thinner beam waist in the sample plane. (c) Intensity profiles in illumination direction for the two Gaussian beams and the lattice illumination. (red, lattice; green, wide Gaussian beam; blue, narrow Gaussian beam)

The beam waist radii of the Gaussian beams were measured using the knife edge method within the sample chamber. The narrow Gaussian beam was adjusted such that its $1/e^2$-waist $\omega_{0,n} = (3.4 \pm 0.3)$ µm corresponded to that of the lattice beams, $\omega_{0,lb} = (3.5 \pm 0.3)$ µm for λ=488 nm. The widths of the lattice beams were determined by directly imaging the beam profiles using the detection pathway and a 45° mirror at the focus position in the sample chamber.

For Gaussian beams L_R and ω_0 are related to each other by

$$L_R = \frac{n\,\pi\,{\omega_0}^2}{\lambda}, \tag{1}$$

where n denotes the refractive index of the medium. Using Eq. (1) the Rayleigh lengths of the profiles could be directly deduced from the beam waist radii. Therefore, the depth of field of

Optics EXPRESS

the focused narrow beam amounted to $2\,x\,L_{R,n}$ =(198 ± 17) µm. The observed qualitative beam profile exhibited the typical maximum at the waist position (5C, blue).

The wide Gaussian beam radius was adjusted to $\omega_{0,w}$ = (5.5 ± 0.3) µm such that its longitudinal intensity profile corresponded to that of the lattice beams over the field of view (Fig. 5(c), green). The field of view achieved with this beam amounted to $2\,x\,L_{R,w}$ = (518 ± 56) µm and was close to that determined for the lattice light-sheet, $2\,x\,L_{R,lb}$ = (535 ± 43) µm. The Rayleigh length of the lattice, $L_{R,lb}$, was estimated by the MATLAB simulation on the basis of the measured beam width, $\omega_{0,lb}$ = (3.5 ± 0.3) µm. All values are summarized in Table 1.

Table 1. Comparison of beam waists, field of view and measured axial resolution.

	Lattice	Wide Gaussian	Narrow Gaussian
ω_0 in water n=1.33	(3.5 ± 0.3) µm	(5.5 ± 0.7) µm	(3.4 ± 0.3) µm
Two-fold Rayleigh length at 488nm, n=1.33	(535 ± 43) µm	(518 ± 56) µm	(198 ± 17) µm
Intensity decrease in propagation direction (Fig. 5(c))	85%	85%	70%
Best axial resolution	(1.2 ± 0.2) µm	(1.4 ± 0.2) µm	(1.2 ± 0.2) µm

The optical resolution is determined by the product of the illumination intensity distribution and the detection point spread function. The theoretical expectation for the FWHM of the axial resolution for a sheet created by scanning of the narrow beam at a detection wavelength of 520 nm using a NA 1.0 objective amounted to 1.07 µm. This value was calculated using the approach presented previously [14,16].

The experimentally realized resolution can be measured using submicron-sized fluorescent beads. Thus, we imaged green fluorescent beads with a diameter D=0.2 µm immobilized in a 1% agarose gel. The refractive index of the 1% agarose gel is close to that of water (n=1.332, [17]). The beads were illuminated by 488 nm laser light using the scanned lattice beams and both Gaussian beams. The respective axial resolutions $FWHM_z$ over the image field were determined by the acquisition and evaluation of image stacks with an axial step size of Δz=0.2 µm. The lateral and axial resolutions were determined as a function of position along the illumination axis by plotting the intensity profiles using Fiji [18] as full width at half maximum (FWHM) of the bead signals, $FWHM_{b,xy}$ and $FWHM_{b,z}$, respectively (Fig. 6(a)). We corrected the measured values for the finite bead size according to $FWHM = \sqrt{FWHM_b^2 - D^2}$. The smallest values for the axial resolution within the illumination fields for the Gaussian beams were observed at the locations of the beam waists, as expected (Fig. 6(b)). The best axial resolutions were obtained for the lattice illumination and for the narrow Gaussian beam, namely $FWHM_z$ = (1.2 ± 0.2) µm. The best axial resolution achieved with the wide Gaussian beam corresponded to $FWHM_z$ = (1.4 ± 0.2) µm.

In summary, our lattice illumination combined the advantages of a large lateral illumination field size featuring a comparatively constant illumination intensity with a small axial sheet thickness, required to achieve optimal axial resolution.

3.4. Imaging of an expanded mouse brain section

In order to evaluate the performance of the constructed lattice light-sheet microscope in large expanded samples of the dorsal dentate gyrus (DG) of a mouse brain, we imaged GFP-labeled granule cells and their neurites to achieve super resolved representations. Briefly, coronal DG sections were prepared for tissue expansion and LSFM analysis from a PROX1-Cre mouse injected with rAAV-DIO-EGFP-WPRE to achieve selective expression of EGFP in DG granule cells [14]. The samples were prepared in the following way. Prox1-Cre transgenic mice were maintained on a 12 hours light/12 hours dark cycle with food and water always available. All the experiments were carried out in accordance with the German animal protection law (TierSCHG), FELASA and were approved by the animal welfare committee of the University of Bonn. Viral

Optics EXPRESS

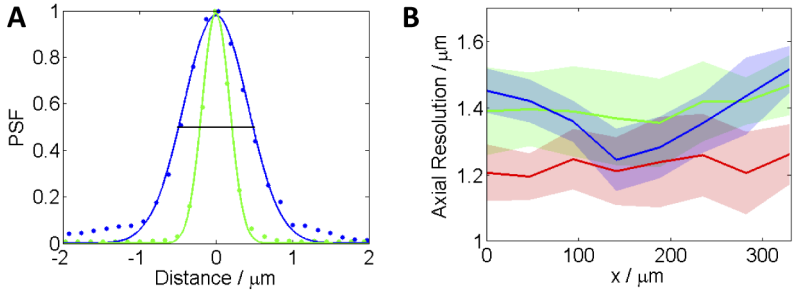

Fig. 6. Axial resolution. (a) Determination of FWHM values of an exemplary bead (blue dotted line, normalized intensity values along the detection axis; green dotted line, normalized intensity values in lateral direction; full line, results of fitting a Gaussian function; FWHM indicated by the black line). (b) Axial resolution as a function of position along the illumination direction. The colored curves show the mean values of N=10 beads in each x-interval, the shaded regions indicate the standard deviations (red, lattice; green, wide Gaussian beam; blue, narrow Gaussian beam)

injections were performed under aseptic conditions in Prox1-Cre mice up to 10 months old. The mice were anesthetized with a mixture of Fentanyl (Rotexmedica, Trittau, Germany), Midazolam (Rotexmedica), and Domitor (Orion Pharma, Hamburg, Germany) via intraperitoneal injection (0.05/5.0/0.5 mg/kg). Analgesia (5 mg/kg of Carprofen) was administered intraperitoneally prior to the injection, and Xylocain (AstraZeneca, Germany) was used for local anesthesia. Stereotactic injections were performed using an injection frame (WPI Benchmark/Kopf) and a microprocessor-controlled minipump (World Precision Instruments, Sarasota, Florida), the viral solution was injected bilaterally into the hippocampus (rAAV-DIO-EGFP-WPRE). After the injection, the scalp was sutured with PERMA-HAND Silk Suture (Ethicon), and an antibacterial ointment (Refobacin, Almirall, Germany) was applied, followed by the intraperitoneal injection of a mixture of Naloxon (B. Braun, Germany), Flumazenil (B. Braun, Germany), and Antisedan (Orion Pharma) (1.2/0.5/2.5 mg/kg). To prevent wound pain, analgesia was administered on the four following days.

After incubation, mice were anesthetized with a mixture of Xylazine (10 mg/kg; Bayer Vital, Germany) and ketamine (100 mg/kg; Bela-pharm GmbH & Co. KG, Germany). Using a peristaltic pump (peristaltic pump PLP33, Mercateo, Germany), the mice were transcardially perfused with phosphate buffered saline (PBS, 137 mM sodium chloride, 2.7 mM potassium chloride, 10 mM di-sodium hydrygen phosphate, 1.8 mM potassium dihydrogen phosphate) followed by 4% paraformaldehyde (PFA) in PBS. Brains were removed from the skull and post-fixed in 4% PFA overnight (ON) at +4°C. After fixation, the brains were moved into PBS containing 0.01% sodium azide and stored at +4°C until sectioning. Fixed brains were sectioned coronally (100 µm) using a vibratome (Leica VT1000 S) and stored in phosphate buffered solution (PBS) containing 0.01% sodium azide at +4 °C.

The expansion microscopy protocol was modified from [19,20]. The sections were incubated with 2 mM methylacrylic acid-hydroxysuccinimide ester (MA-NHS) (Sigma Aldrich) for 2 h on a shaker at room temperature. After washing three times in PBS, the sections were incubated for 1.5 hours in the monomer solution (8.6% sodium acrylate, 2.5% acrylamide, 0.15% N,N'-methylenebisacrylamide, 11.7% NaCl in PBS) on a shaker at +4°C. The sections were transferred to the gelling chamber, followed by 2 h incubation at 37°C in a gelling solution for polymerization. The gelling solution was prepared by adding 4-Hydroxy-2,2,6,6-tetramethylpiperidine 1-oxyl (4-hydroxy-TEMPO, 0.01%), N,N,N′,N′-tetramethylethylenediamine (TEMED, 0.2%), and ammonium persulfate (0.2%) to the monomer solution. After gel formation, the samples were

Optics EXPRESS

incubated at 37°C for 16 hours in digestion buffer (50 mM Tris, 1 mM EDTA, 0.5% Triton-X100, 0.8 M guanidine hydrochloride and 16 U/ml of proteinase K; pH 8.0). The next day, the digestion buffer was removed and the sections were washed three times with PBS.

Then, the digested brain sections were incubated in blocking buffer (PBS containing 0.1% TritonX-100 and 5% bovine serum albumine) on a shaker for 5 h at room temperature to prevent unspecific binding of the primary antibody. After blocking, the sections were incubated for 24 h with the primary antibody (chicken anti-GFP; 1:500 in blocking buffer; Abcam, ab13970) on a shaker at low speed at +4°C. The following day, the sections were washed at room temperature in blocking buffer three times for 20 minutes and incubated for 24 h in Alexa Fluor 488-conjugated goat antibody against chicken IgY (H + L, 1:400 in blocking buffer; Invitrogen, A-11039) on a shaker at +4°C. For cell nuclear staining, the sample was incubated 3 h in a solution of 0.5 µg/mL 4′,6-diamidine-2′-phenylindole dihydrochloride (DAPI) in water.

For imaging, the expanded gel samples were fixed on a coverslip with poly-L-lysine to avoid movements during the measurements. A quick control of a successful sample preparation was performed using a confocal laser scanning microscope (LSM 880, Carl Zeiss Microscopy). Then, the coverslip was screwed on a sample holder arm and mounted in the imaging chamber as explained above. The chamber was filled with deionized water.

Note, that the antibody staining against EGFP was performed after the digestion step, which greatly improved the tissue permeability and reduced non-specific binding effects. Image acquisition was accomplished using a single frame exposure time of 30 ms. Altogether, acquisition of a stack of 2000 frames took 143 s which corresponds to a frame rate of 14 Hz.

The sample size greatly exceeded the lateral object field size of $(333\,\mu m)^2$. Therefore, the data were acquired in a tiled manner. Volumetric data of the expanded mouse brain slices were acquired by moving the sample through the light sheet. Figure 7(a) shows a volume rendering of a single neuron, which was imaged using 16 single stacks with 2120 images each and 10% lateral overlap between adjacent stacks and z-steps of 400 nm to fulfill the Nyquist criterion. The sample was illuminated using an excitation wavelength of 488 nm. The complete imaged volume has a size of $1.2 \times 1.2 \times 0.8$ mm^3. Since the sample was expanded by a factor of approximately 4, this corresponded to a size of $0.3 \times 0.3 \times 0.2$ mm^3. After imaging the tile stacks were stitched using Imaris 9.5.1 (Bitplane AG, Zurich, Switzerland) and contrast adjusted. To this end, the intensity histograms were adjusted to homogenize brightness and contrast throughout the complete data set. Every 3D stack was first scanned to find its minimum and maximum intensity values. With the respective values a linear intensity adjustment was performed to cover the full dynamic range.

The volumetric image data shows an expanded DG neuron and its neurites. Figure 7(b) shows a rendered branched neurite from the red square marked region in Fig. 7(a). Note that tiny details and fine dendritic structures can be recognized in high resolution.

A maximum intensity projection of a stack comprising 200 images of a dendrite is shown in Fig. 7(c). Individual spines as well as thin spine necks can be well resolved. Figure 7(d) shows a magnification of the marked field in Fig. 7(c). Finally, Fig. 7(e) shows the intensity profile of a spine neck marked by a red line in the close up view in Fig. 7(d). The full width at half maximum (FWHM) of the spine intensity profile amounted to 640 nm, which corresponds to 160 nm considering the expansion factor of 4 and is thus well below the optical diffraction limit.

For calculation of z-projections, the maximum intensity projection algorithm of Fiji was used. Three-dimensional representation of data was achieved using the Surpass view in Imaris. Data processing was performed on a workstation equipped with an Intel Xeon Gold 6128 CPU (3.40 GHz, 6 cores), 512 GB memory and a Nvidia Geforce GTX 980 GPU running under Windows 10 Pro.

Optics EXPRESS

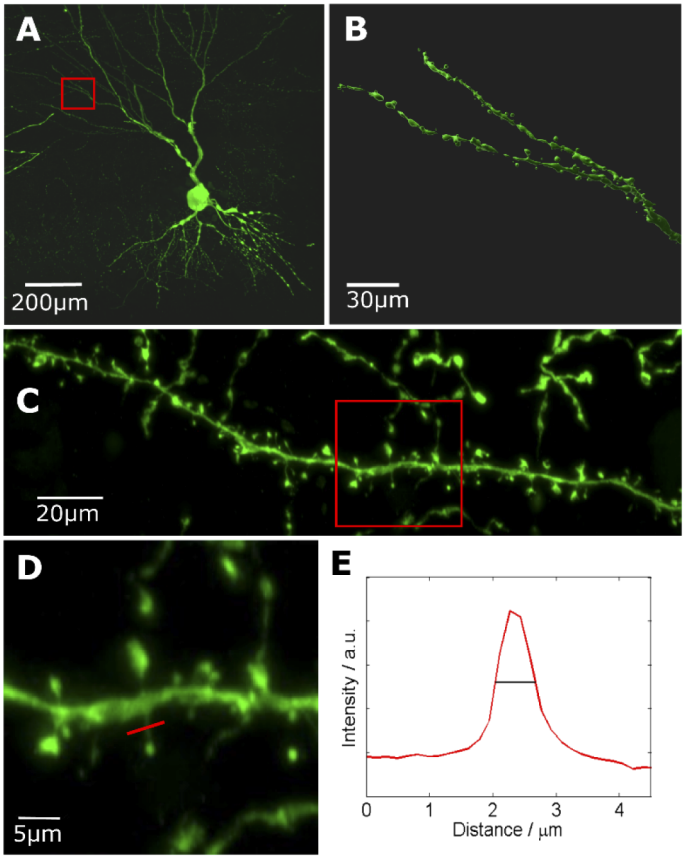

Fig. 7. Antibody stained expanded mouse brain section imaged with the lattice light-sheet. (a) Large stitched volume showing a neuron inside the mouse hippocampus. (b) The close-up shows a rendered dendrite where fine details are resolved. (d) Close up of the dendritic spines marked by the red box in (c). (e) Intensity profile of the spine neck marked with the red line in (e). The black line marks the FWHM with a length of 640 nm. All scales refer to expanded samples.

3.5. Dual-color imaging

The setup was equipped with two sCMOS cameras and a beam-splitter for simultaneous dual camera imaging. This was demonstrated by green fluorescent granule cells labeled by an Alexa488-immunostaining against EGFP and staining of cell nuclei using the UV-excitable dye DAPI. A specimen volume was imaged in 20 tiles with 1630 images each, an axial step size of 400 nm and 10% lateral overlap. The complete sample size amounted to $1.5 \times 1.2 \times 0.6$ mm^3, which corresponded to a true size of $0.38 \times 0.3 \times 0.15$ mm^3 before expansion. Figure 8(a) shows a volume rendering of the stitched and contrast-adjusted DAPI channel (pink) excited with 405 nm and the Alexa488 channel (green) excited with 488 nm. A network of four granule cells is visible together with the surrounding cell nuclei. Figure 8(b) shows a single frame of a stack to highlight the specific overlay of the cell and its DAPI stained cell nucleus.

3.6. Comparison of resolution

To validate the performance of our LLSFM in comparison to a standard Gaussian light-sheet microscope, a stack of the same region inside the expanded mouse hippocampus was acquired

Optics EXPRESS

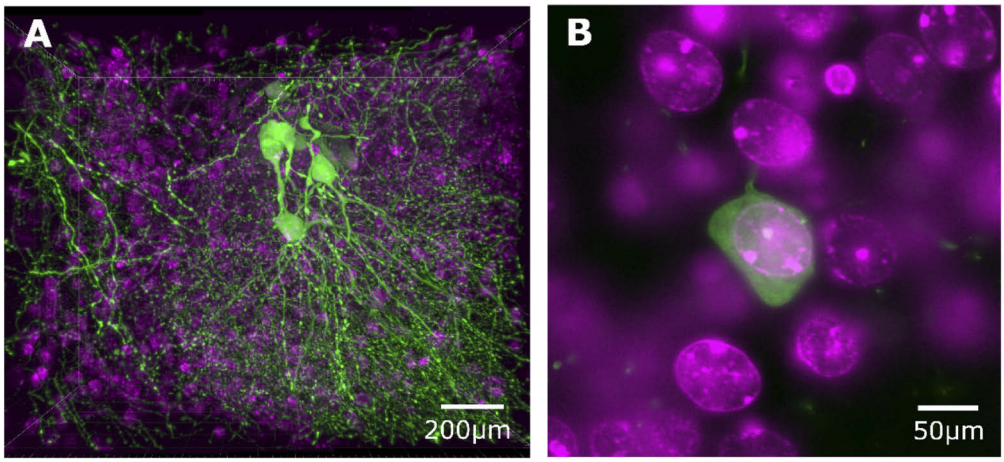

Fig. 8. Two-color imaging of a set of granule cells in an expanded mouse brain hippocampus section. (a) Large volume showing immunostained EGFP-expressing granule cells and dendrites (green) as well as cell nuclei stained by DAPI (pink) excited with 488 and 405 nm, respectively. (b) A single frame of the stack showing the overlay of the cell nucleus and the soma.

using both methods. Here, the z-step size was 300 nm. Figures 9(a) and (b) show the maximum projection of a stack with 1160 images acquired with the lattice light-sheet and the Gaussian

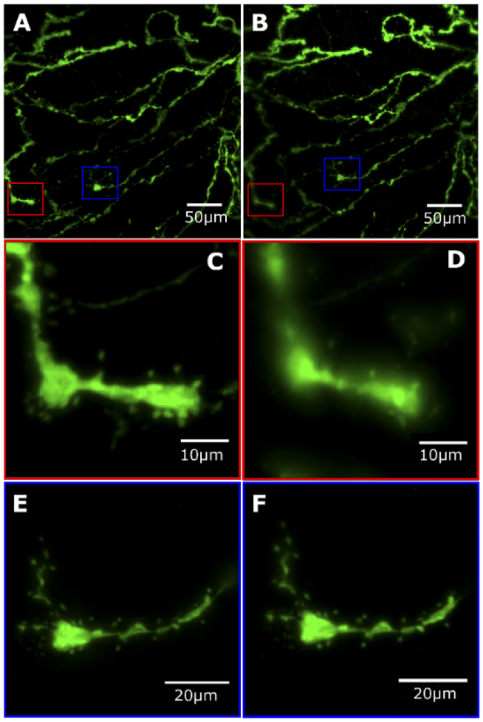

Fig. 9. Maximum intensity projections of dendrites in an expanded mouse hippocampus. (a, c, e): Lattice, (b, d, f): Gaussian. The divergence of the Gaussian beam generates blurred areas at image edges (red box). In the image center the Gaussian beam illumination reaches the resolution of the lattice (blue box).

Optics EXPRESS

light-sheet (w_0=3.4 ± 0.3 µm), respectively. The blue and red marked regions were chosen to compare the resolution of both methods at the image edge (blue box) and image center (red). While the Gaussian light-sheet setup yielded the same image quality in terms of resolution compared to the lattice light-sheet setup in the center of the image (compare Figs. 9(e) and (f)), the resolution decreases significantly at the image edges (compare Figs. 9(c) and (d)). Clearly, the lattice light-sheet illumination featured a constant and high resolution over the complete field of view.

4. Discussion

In contrast to conventional light-sheet microscopy employing scanned Gaussian beams for light sheet generation, lattice light-sheet microscopy features a low diverging light sheet with a homogeneous thickness formed by an array of Bessel-Gaussian beams.

We developed and characterized a rather simple and facile, purpose-built lattice light-sheet microscope based on a high precision hardware mask for lattice light-sheet generation. This custom-made mask containing three light slits generated with CNC milling was positioned in a conjugated plane of the back focal plane of the illumination objective. Our microscope setup combines both, a Gaussian and a lattice light-sheet illumination path allowing us to directly compare the features of both methods on the same sample. Notably, the characterization of the generated light lattice in dye-water solutions confirmed the results of prior simulations and thus proved that our method is applicable to simultaneous multicolor imaging due to the highly constant z-position of the lattice for different excitation wavelengths.

To thoroughly compare the performance of the lattice light-sheet microscope to our conventional LSFM setups, two Gaussian beams with different characteristics were used. First, a narrow Gaussian beam with a similar waist diameter as the lattice beams. This beam yielded the same axial resolution of (1.2 ± 0.2) µm at its focus, but the strong divergence of this Gaussian beam caused an inhomogeneous excitation intensity along the illumination direction, which led to a decrease of the axial resolution at the edges of the field of view. Second, a wide Gaussian beam, whose two-fold Rayleigh length approximated the field width of view of the lattice beams, however, featured a larger diameter which resulted in a lower axial resolution. Finally, the lattice light-sheet excitation combined a comparatively homogeneous illumination and a small axial extension which resulted in a high axial resolution. We conclude that the lattice light-sheet microscope offers the possibility for an increased usable field of view (FOV) combined with high resolution.

Compared to the LLSFM configuration by Chen et al [13]. our setup comprised no spatial light modulator (SLM). Thus, an electronic control and complex programming of the SLM is not required and therefore the overall costs for building a lattice light-sheet microscope are significantly reduced and, most notably, the optical setup using a hardware mask for lattice generation is rather straightforward. Furthermore, the aluminum plate withstands higher irradiances than a spatial light modulator, which might prove useful when combining it with pulsed light excitation. However, using a mask for lattice generation has the disadvantage that the mask light transmission is only 6% of the input light, although the incoming laser light was already transformed into a ring shape by the axicons in order to reduce light losses. Therefore, high laser power is required to achieve an adequate fluorescence excitation of the sample.

As a demonstration of the applicability of our setup, we imaged neuronal networks within expanded mouse brain samples allowing us to test its performance in imaging fine and densely packed details over large scales. We imaged mouse brain samples containing labelled EGFP-expressing granule cells additionally labeled with an antibody against EGFP to increase fluorophore density. We also used DAPI to stain the surrounding cell nuclei to demonstrate the possibility of high-resolution double color imaging. In contrast to our previous protocol [14] we here established a modification of the expansion protocol. To improve the permeability of the sample for the

Optics EXPRESS

antibody we performed the antibody staining after sample digestion. This resulted in a rather isotropic antibody distribution within the sample and also reduced nonspecific binding. It is noteworthy to state that this approach demands a careful optimization of tissue digestion duration in order to avoid a complete destruction of the epitopes.

With our instrument, a maximum frame rate of 14 Hz was reached. A transparent sample volume of 1 mm^3 was imaged in less than 40 min while obeying the Nyquist criterion, which is significantly faster compared to our conventional setup [14]. The homogeneous excitation of the lattice light-sheet lead to a substantially increased usable field of view. In contrast a Gaussian light-sheet with the same waist diameter showed blurred structures at the image borders. This is especially important for fast imaging of large fluorescently labeled brain samples. In fact, sparsely labelled neuronal circuits, eventually spanning an entire mouse brain can theoretically be imaged in less than 3 days. Note that an observation of granule cells and their fine neurites with dendritic spines and spine necks was straightforward with negligible bleaching. Moreover, our lattice light-sheet microscope proved to be well suited for dual-color imaging.

In summary, we demonstrated that a hard-wired lattice light-sheet microscope provides a good alternative to a conventional Gaussian light-sheet microscope. Our setup presented here represents a robust and cost-effective version of a lattice light-sheet microscope and allows fast imaging of large samples at high-resolution.

Funding

Deutscher Akademischer Austauschdienst (to JERG); Comisión Nacional de Investigación Científica y Tecnológica (to JERG); Deutsche Forschungsgemeinschaft (INST 217/886-1, KU 2474/13-1, SCHW 1578/2-1).

Disclosures

The authors declare no conflicts of interest.

References

1. R. M. Power and J. Huisken, "A guide to light-sheet fluorescence microscopy for multiscale imaging," Nat. Methods **14**(4), 360–373 (2017).
2. A.-K. Gustavsson, P. N. Petrov, and W. E. Moerner, "Light sheet approaches for improved precision in 3D localization-based super-resolution imaging in mammalian cells [Invited]," Opt. Express **26**(10), 13122–13147 (2018).
3. S. Corsetti, F. Gunn-Moore, and K. Dholakia, "Light sheet fluorescence microscopy for neuroscience," J. Neurosci. Methods **319**, 16–27 (2019).
4. E. Baumgart and U. Kubitscheck, "Scanned light sheet microscopy with confocal slit detection," Opt. Express **20**(19), 21805–21814 (2012).
5. L. Silvestri, A. Bria, L. Sacconi, G. Iannello, and F. S. Pavone, "Confocal light sheet microscopy: micron-scale neuroanatomy of the entire mouse brain," Opt. Express **20**(18), 20582–20598 (2012).
6. P. J. Keller, A. D. Schmidt, J. Wittbrodt, and E. H. K. Stelzer, "Reconstruction of zebrafish early embryonic development by scanned light sheet microscopy," Science **322**(5904), 1065–1069 (2008).
7. T. V. Truong, W. Supatto, D. S. Koos, J. M. Choi, and S. E. Fraser, "Deep and fast live imaging with two-photon scanned light-sheet microscopy," Nat. Methods **8**(9), 757–760 (2011).
8. T. A. Planchon, L. Gao, D. E. Milkie, M. W. Davidson, J. A. Galbraith, C. G. Galbraith, and E. Betzig, "Rapid three-dimensional isotropic imaging of living cells using Bessel beam plane illumination," Nat. Methods **8**(5), 417–423 (2011).
9. F. O. Fahrbach and A. Rohrbach, "Propagation stability of self-reconstructing Bessel beams enables contrast-enhanced imaging in thick media," Nat. Commun. **3**(1), 632 (2012).
10. T. Vettenburg, H. I. C. Dalgarno, J. Nylk, C. Coll-Lladó, D. E. K. Ferrier, T. Čižmár, F. J. Gunn-Moore, and K. Dholakia, "Light-sheet microscopy using an Airy beam," Nat. Methods **11**(5), 541–544 (2014).
11. M. Friedrich, Q. Gan, V. Ermolayev, and G. S. Harms, "STED-SPIM: Stimulated emission depletion improves sheet illumination microscopy resolution," Biophys. J. **100**(8), L43–L45 (2011).
12. Y. Wan, K. McDole, and P. J. Keller, "Light-Sheet Microscopy and Its Potential for Understanding Developmental Processes," Annu. Rev. Cell Dev. Biol. **35**(1), 655–681 (2019).

Optics EXPRESS

13. B.-C. Chen, W. R. Legant, K. Wang, L. Shao, D. E. Milkie, M. W. Davidson, C. Janetopoulos, X. S. Wu, J. A. Hammer, Z. Liu, B. P. English, Y. Mimori-Kiyosue, D. P. Romero, A. T. Ritter, J. Lippincott-Schwartz, L. Fritz-Laylin, R. D. Mullins, D. M. Mitchell, J. N. Bembenek, A.-C. Reymann, R. Böhme, S. W. Grill, J. T. Wang, G. Seydoux, U. S. Tulu, D. P. Kiehart, and E. Betzig, "Lattice light-sheet microscopy: imaging molecules to embryos at high spatiotemporal resolution," Science **346**(6208), 1257998 (2014).
14. J. Bürgers, I. Pavlova, J. E. Rodriguez-Gatica, C. Henneberger, M. Oeller, J. A. Ruland, J. P. Siebrasse, U. Kubitscheck, and M. K. Schwarz, "Light-sheet fluorescence expansion microscopy: fast mapping of neural circuits at super resolution," Neurophotonics **6**(01), 1 (2019).
15. K. L. Ellefsen and I. Parker, "Dynamic Ca2+ imaging with a simplified lattice light-sheet microscope: A sideways view of subcellular Ca2+ puffs," Cell Calcium **71**, 34–44 (2018).
16. J. G. Ritter, R. Veith, J. P. Siebrasse, and U. Kubitscheck, "High-contrast single-particle tracking by selective focal plane illumination microscopy," Opt. Express **16**(10), 7142–7152 (2008).
17. A. Jain, A. H. J. Yang, and D. Erickson, "Gel-based optical waveguides with live cell encapsulation and integrated microfluidics," Opt. Lett. **37**(9), 1472–1474 (2012).
18. J. Schindelin, I. Arganda-Carreras, E. Frise, V. Kaynig, M. Longair, T. Pietzsch, S. Preibisch, C. Rueden, S. Saalfeld, B. Schmid, J.-Y. Tinevez, D. J. White, V. Hartenstein, K. Eliceiri, P. Tomancak, and A. Cardona, "Fiji: an open-source platform for biological-image analysis," Nat. Methods **9**(7), 676–682 (2012).
19. F. Chen, P. W. Tillberg, and E. S. Boyden, "Optical imaging. Expansion microscopy," Science **347**(6221), 543–548 (2015).
20. T. J. Chozinski, A. R. Halpern, H. Okawa, H.-J. Kim, G. J. Tremel, R. O. L. Wong, and J. C. Vaughan, "Expansion microscopy with conventional antibodies and fluorescent proteins," Nat. Methods **13**(6), 485–488 (2016).